Lamb wave damage imaging method based on multimodal dispersion compensation and compressive sensing

Yuan Chen[1,2,*], Wenbin Liu[3], Guangming Zhang[4], Xin Su[3], Hongwei Ma[2,3], Xiang Wan[2,3], Ming Dong[2,3]

1College of Sciences, Xi'an University of Science and Technology, Xi'an, Shaanxi, 710054, China

2Shaanxi Key Laboratory of Mine Electromechanical Equipment Intelligent Detection and Control, Xi'an University of Science and Technology, Xi'an, Shaanxi, 710054, China

3College of Mechanical Engineering, Xi'an University of Science and Technology, Xi'an, Shaanxi,710054, China

4School of Engineering, Liverpool John Moores University, Byrom Street, L3 3AF, United Kingdom

**Corresponding email: chenyuan1030@xust.edu.cn*

Abstract: To address the challenges of wave packet broadening and signal distortion caused by multimodality and dispersion effects in Lamb wave-based damage detection for carbon fiber reinforced polymer (CFRP) laminates, this paper proposes an imaging method that combines multimodal dispersion compensation and compressive sensing (CS). First, the Rayleigh-Lamb equation is solved using the T300/5028 material parameters to establish the dispersion characteristic model. A baseline-free multimodal dispersion compensation technique is developed for performing frequency-domain phase correction and time-domain signal reconstruction, allowing accurate estimation of the compensation distance between each sensor and the damage. Subsequently, a CS-based imaging algorithm that fuses delay-and-sum (DAS) and sparse reconstruction is proposed and verified using finite-element simulations and experimental tests. The results show maximum localization errors of 2.03±0.05mm in simulations and 2.31±0.56mm in experiments. This work provides theoretical insights and experimental support for the high-precise identification of delamination damage in anisotropic composite materials.

Keywords: multimodal dispersion compensation; phase compensation; compressive sensing; high-precision detection; Lamb wave imaging

1 Introduction

Ultrasonic Lamb wave testing is an effective method in non-destructive testing (NDT)[1-4], structural health monitoring (SHM) [5 ,6] and material characterization [7] . Lamb waves have been extensively employed in the structural health monitoring of plate-like components due to their capacity for long-range propagation and wide-area coverage. This makes them particularly well-suited to inspecting CFRP laminates. However, the anisotropic nature of CFRP laminates cause multimode propagation and significant dispersion during Lamb wave transmission. These phenomena considerably compromise accuracy of damage localization, the reliability of quantitative evaluation and spatial resolution of resultant images. Therefore, developing high-precision dispersion compensation methods capable of achieving time-domain focusing and waveform reconstruction of multimode signals is crucial for improving the overall performance of Lamb wave-based NDT.

In the recent years, various dispersion compensation methods have been introduced in literatures. Li et al. [8] presented a Lamb wave dispersion compensation method based on the measured wavenumber (ΔK-DC), which validates the consistency between the theoretical and measured wavenumbers by using relative wavenumber measurement, propagation distance estimation, phase compensation and Lamb wave correction. Wilcox et al. [9] proposed a time-

distance mapping method that utilizes fast Fourier transform (FFT) and wavenumber interpolation to convert signals from the time domain to the distance domain. Extending this work, Cai et al. [10] introduced a linearization framework offering two compensation schemes: linear dispersion signal construction (LDSC) and non-dispersion signal construction (NDSC). Jochen et al. [11] adopted wave packet tracking to accurately extract the time-of-flight (ToF), thereby enabling high-resolution damage imaging. Zhang et al. [12] developed a Lamb wave dispersion compensation method based on convolutional autoencoders, in which the model establishes a mapping relationship between dispersed signals and wave-packet flight times, and reconstruct the dispersion-compensated signals by integrating the network-estimated ToF with the excitation waveform enables. Li et al. [13] proposed a nonlinear group-delay estimation-based dispersion compensation method that achieves compensation via time-frequency ridges, even when the dispersion curve is unavailable. Ling et al. [14] introduced the wideband dispersion reversal (WDR) method, which enhances imaging quality through a combination of modal separation and self-compensation mechanism. De Marchi et al. [15] applied a warped frequency transform for dispersion compensation; however, residual signal distortion remains due to the inherent limitations of the nonlinear warping function. Zeng et al. [16] proposed a dispersion compensation method based on chirp technology, which reduces dispersion the effects of dispersion by pre-compensating the original narrowband excitation signal for dispersion. This allows the temporal duration of the received wave packet to be compressed during extraction. Using this method makes it possible to readily identify closely spaced structural features in the time domain. Xu et al. [17] constructed a dispersion dictionary based on CS theory to achieve dispersion compensation under a sparse-representation framework. Although existing dispersion compensation methods demonstrate considerable potential for application, they still have several significant limitations. Firstly, the performance of most methods relies heavily on prior knowledge, necessitating accurate time-frequency analysis of dispersion characteristics or reference signals. However, in actual anisotropic composite structures, such prior information is also difficult to obtain under varying environmental conditions. Secondly, existing methods provide insufficient compensation integrity when dealing with complex anisotropic materials and non-ideal boundary conditions. Furthermore, when addressing inspection demands involving diverse structures and complex damage types in practical engineering scenarios, existing methods are neither accurate nor reliable enough. To overcome dispersion-related signal distortion and modal overlap and to improve damage-detection precision, extensive work has been devoted to Lamb-wave imaging algorithms, leading to multiple methods for damage localization and visualization.

In realm of damage image and localization using Lamb waves, several advanced methodologies have been developed to enhance detection performance. Su et al. [18] developed a damage identification approach based on Hilbert spectral analysis and Lamb wave tomography. This enables localized imaging of single and multiple defects in CFRP laminates. Kai et al. [19] proposed a baseline-free imaging framework combining adaptive time reversal and a nonlinear-exponential reconstruction algorithm (NE-RAPID) to enhance the accuracy of traditional RAPID for the probabilistic detection of delamination. Meanwhile, Migot et al.[20] introduced an imaging technique that integrates synthetic time-reversal concepts with Gaussian distribution functions. This technique revealed directional scattering effects and suggested optimal transducer–sensor layouts in simulations. Similarly, Renéet et al. [21] presented a Fourier-domain synthetic-aperture focusing technique (F-SAFT) that accounts for Lamb-wave dispersion. This allows for defect detection in the highly dispersive region of the fundamental S_0 mode, demonstrating high localization accuracy

on CFRP specimens. Wang et al. [22] employed a nonlinear defect index coupled with an adaptive weighting algorithm that uses the relative nonlinearity coefficient of Lamb waves to improve the detection of small defects in CFRP laminates. Xu et al. [23] introduced a Lamb wave imaging method that uses frequency-domain multi-frequency sparse decomposition and is designed for localizing damage in isotropic plate-like structures. This method involves collecting scattered wave signals using a sensor array, extracting frequency-dependent scattering coefficients via point-by-point sparse decomposition and reconstructing the damage by fusing multi-frequency scattering features. Müller et al. [24] proposed a damage imaging method for CFRP laminates based on the total focusing method (TFM) and full matrix capture (FMC) post-processing. By optimizing image filtering algorithms, this method effectively suppressed artefacts in signal processing, enabling clear visualization of damage contours and facilitating assessment of their location and dimensions. Cui et al. [25] developed a reference-free Lamb wave damage localization method which extracted damage-scattered waves through frequency-wavenumber spectral analysis, integrating probabilistic imaging algorithms for spatial damage mapping. Using a piezoelectric transducer array, this method acquired wavefield data at sub-Nyquist sampling rates and reconstructed the original wavefield via CS, significantly enhancing data acquisition efficiency. Perelli et al. [26] proposed a CS-based imaging method for ultrasonic signal decomposition. This method used a warped frequency transform-based sparse dictionary to compensate for dispersion effects and combined this with sparse reconstruction techniques to achieve high-resolution damage detection. Its effectiveness was validated experimentally on aluminum plates. Despite advances in existing imaging methods, there are still several significant limitations to their application in practical engineering scenarios. Firstly, the high computational complexity of imaging methods often means that current approaches cannot meet real-time detection requirements. Furthermore, existing imaging methods tend to have low resolution and positioning accuracy when detecting multiple small defects or defects near structural boundaries. Environmental noise, sensor placement constraints, and structural geometric complexity also significantly impact the stability and reliability of imaging results.

Current approaches lack a unified framework that can address multimodal dispersion compensation, anisotropic wave propagation, and sparse reconstruction, while also enabling baseline-free detection. To overcome these limitations, this paper proposes a Lamb wave damage imaging method that integrates dispersion compensation with CS. First, a dispersion compensation algorithm based on propagation distance is employed to reconstruct Lamb wave signals in the time domain. This accurately estimates the compensated distance between each sensor and the damage. Secondly, a CS imaging algorithm is designed by integrating DAS with sparse reconstruction. This significantly improves localization accuracy while maintaining computational efficiency. Finally, simulations and experiments are conducted to verify the effectiveness and superiority of the proposed method.

2. Theoretical foundations and methods

2.1 Lamb wave frequency dispersion compensation

In Lamb wave detection, energy propagation is primarily governed by group velocity, so dispersion compensation is performed based on group velocity. The time-domain sensor signal. $S(t)$ is converted into the frequency domain using the discrete Fourier transform (DFT), expressed as [27] :

$$S(f) = \boldsymbol{F}\{S(t)\} = \sum_{n=0}^{N-1} S(n\Delta t) \cdot e^{-j2\pi f_n \Delta t} \tag{1}$$

where $\boldsymbol{F}\{\bullet\}$ denotes Fourier transform operator, N is number of sample points, Δt represents sampling interval, f is the frequency component.

The frequency-domain propagation model is described by the following equations:

$$\begin{aligned} U(f,d) &= S_0(f) \times H(f,d) \\ H(f,d) &= A(f,d)e^{-jk(f)d} \end{aligned} \tag{2}$$

$$k(f) = 2\pi f / C_p(f) \tag{3}$$

where $U(f,d)$ represents the frequency spectrum of acquired signal after transmission distance d, $S_0(f)$ is frequency spectrum of original signal, $H(f,d)$ is transfer function, $A(f,d)$ is the attenuation factor, j is imaginary unit, $k(f)$ is wavenumber，and $C_p(f)$ is group velocity of Lamb waves. The phase of the dispersion compensation can be calculated by [9] :

$$\varphi_{comp}(f,\theta) = 2\pi f_k \cdot (\frac{1}{C_g(f,\theta)} \frac{1}{C_{ref}}) \cdot d(\lambda) \tag{4}$$

where $\varphi_{comp}(f,\theta)$ represents the phase requiring compensation, $C_g(f,\theta)$ is the real-time group velocity of Lamb waves at frequency f, and C_{ref} is the selected reference group velocity. The phase requiring compensation can be found by interpolating between these two values. In orthotropic composite materials, the group velocity of Lamb waves varies significantly depending on the propagation direction. The group velocity function can be expressed as follows:

$$C_g(f,\theta) = c_g^{(0)}(f) + \sum_{n=1}^{N} [a_n(f)cos(2n\theta) + b_n(f)sin(2n\theta)] \tag{5}$$

where θ the angle between the propagation direction and the material's principal axis; $c_g^{(0)}(f)$ is the anisotropic fundamental frequency term; $a_n(f)$ and $b_n(f)$ are the directional harmonic coefficients, obtained by solving the Rayleigh-Lamb equation for different directions.

The propagation path distance for dispersion compensation is a key parameter influencing the accuracy of the compensation. Since the damage location is unknown during detection, this paper uses a ray-theory-based path-searching algorithm to calculate the effective wave propagation distance. The problem is formulated into optimization task, with the objective function defined as follows:

$$d(\lambda) = arg\min_{\mathrm{d}} S\left[\lambda \cdot K(S_{comp}(t;d)) + (1-\lambda) \cdot H(S_{comp}(t;d))\right] \tag{6}$$

where $s_{comp}(t;d)$ denotes the compensated time-domain signal, which depends on the compensation distance $d(\lambda)$; $H(S_{comp}(t;d))$ represents the information entropy of a signal, characterizing the dispersion of its energy distribution, with lower values indicating greater energy concentration; $K(S_{comp}(t;d))$ denotes the signal's kurtosis ,reflecting the sharpness of its amplitude distribution, with higher values corresponding to steeper wavefronts. The weighting coefficient λ is selected based on the relative importance of signal entropy and kurtosis in the optimization

objective. Minimizing entropy promotes energy concentration, while maximizing kurtosis favors sharp wave packets. To balance these two aims, a grid search over λ (0.1–0.9, step 0.1) is conducted on simulation data, using the peak-to-energy ratio (PER) of the compensated signal as the evaluation criterion.

$$PER(\lambda) = \frac{max\left|S_{comp}(t;d(\lambda))\right|}{\sqrt{\frac{1}{N}\sum_{t=1}^{N} S_{comp}^2(t;d(\lambda))}} \tag{7}$$

where $S_{comp}(t;d(\lambda))$ denotes the compensation signal obtained by introducing the optimal compensation distance, which is calculated by substituting the optimal weight coefficient into Eq. (6). The focusing index PER of the compensated signal using simulation data for different values of λ (0.1–0.9). The standard deviation in the table indicates the fluctuation range of the PER values obtained from numerical simulations. When λ = 0.5, PER reaches its maximum, indicating optimal compensation performance (see Table 1). This finding is further validated using experimental data, which confirms its robustness.

Table 1 The PER values and their standard deviations at different λ values.

λ value	0.1	0.2	0.3	0.4	0.5	0.6	0.7	0.8	0.9
PER value	0.65	0.72	0.78	0.85	0.92	0.88	0.82	0.75	0.68
Standard deviation	±0.042	±0.041	±0.039	±0.035	±0.045	±0.032	±0.034	±0.035	±0.044

This optimization objective is to find the optimal distance $d(\lambda)$ that maximizes signal energy concentration and wave packet sharpness by minimizing signal entropy and maximizing signal kurtosis. After determining the optimal compensation distance, the phase-compensated frequency-domain signal can be restored to the time-domain using an inverse Fourier transform [28] :

$$S_{comp}(t) = \boldsymbol{F}^{-1}\{S_{comp}(f)\} = \frac{1}{N}\sum_{k=0}^{N-1} S_{comp}(f_k)\cdot e^{j2\pi f_k\left(\frac{1}{C_g(f,\theta)}-\frac{1}{C_{ref}}\right)d(\lambda)}\cdot e^{j2\pi f_k t} \tag{8}$$

This process compensates for dispersion by applying frequency-dependent phase compensation to each frequency component in the frequency domain, resulting in a time-domain input signal that is well-focused and suitable for subsequent high-precision imaging.

2.2 Fusion imaging method

This paper proposes a CS-based fusion imaging algorithm, which integrates DAS stacking, sparse reconstruction and dispersion compensation in order to achieve high-definition imaging and localization of the target damage lesion. This algorithm employs the DAS imaging results as the base contour and the sparse imaging results as the high-resolution weighting map. An adaptive weighted fusion scheme is then applied to enhance image detail, which can be expressed mathematically as follows [29 ,30] :

$$I_{DAS}(r) = \sum_{p=1}^{P}\left|S_{comp}(t_p(r))\right| \tag{9}$$

$$I_{CS}(r) = \sum_{\mathrm{p}=1}^{\mathrm{p}} w_p(r)\cdot\left|S_{comp}(t_p(r))\right|^2 \tag{10}$$

$$I_{Fused}(r) = I_{DAS}(r)^{1-\gamma} \cdot \left(I_{CS}(r)\right)^{\gamma} \tag{11}$$

where $t_p(r)$ represents the theoretical propagation time for signal to travel the *p*-th path to pixel *r*, while $S_{comp}(t)$ is time domain signal of same path after dispersion compensation; $w_p(r)$ is a Gaussian weighting factor that decreases with propagation distance, which is used to suppress noise and interference from distant paths, thereby focusing energy more effectively on the potential damage region; $\left|S_{comp}(t_p(r))\right|^2$ enhances the target signal energy by squaring its amplitude, thus improving contrast against the background; γ denotes the fusion coefficient, which controls the degree of detail enhancement introduced by sparse imaging. A higher γ value yields stronger detail enhancement, whereas an excessively low γ value reduce the fusion effect to a level similar to DAS imaging. This study determines the optimal γ value using an adaptive contrast enhancement function, defined as:

$$Contrast(\gamma) = \frac{\mu_{damage} - \mu_{background}}{\sigma_{background}} \tag{12}$$

where μ_{damage} and $\mu_{background}$ denote the mean pixel values of the damaged region and background region respectively, and $\sigma_{background}$ is the standard deviation of the background region. Using the simulation data, γ is varied from 0 to 1 (step 0.1), and the contrast of the fusion image is evaluated for each γ value. The standard deviation in the table indicates the fluctuation range of the *Contrast* values obtained from independent simulations under identical conditions. The highest contrast is achieved at γ=0.7 (see Table 2), where the fused result substantially enhances the detail-resolving ability of CS imaging while retaining DAS structural information. Therefore, $\gamma = 0.7$ is adopted throughout this study and validated across both simulation and experimental data.

Table 2 The Contrast and its standard deviation at different γ values.

γ value	0.1	0.2	0.3	0.4	0.5	0.6	0.7	0.8	0.9
Contrast value	0.35	0.46	0.58	0.72	0.85	0.88	0.92	0.86	0.78
Standard deviation	±0.040	±0.035	±0.037	±0.042	±0.033	±0.037	±0.034	±0.041	±0.028

The theory of CS shows that if signal is sparse in a specific transformation domain, it can accurately be reconstructed from a significantly smaller set of measurements sampled at a rate below the Nyquist frequency. In damage imaging, the spatial distribution of damaged regions is inherently sparse, thus fulfilling the fundamental requirement for CS. To efficiently achieve sparse reconstruction, this paper uses iterative soft-thresholding algorithm (ISTA) to solve the basis pursuit denoising problem. The core iterative step is formulated as follows [31] :

$$x^{(k+1)} = S_{\lambda\alpha}(x^{(k)} - \alpha \mathrm{A}^T(\mathrm{A}x^{(k)} - y)) \tag{13}$$

where S_λ denotes the soft-thresholding operator, $(\mathrm{A}x^{(k)} - y)$ represents the residual term that characterizes the deviation between reconstructed and measured data, A^T is the gradient that maps the residual to image space, and α is the step size that controls the magnitude of each iterative update. The main advantage of this method lies in its reliance on measurement data from only a limited number of sensor paths, which substantially reduces the amount of data required for acquisition. At the same time, the imposed sparsity constraints effectively suppress noise and

artefacts, thereby enhancing accuracy, robustness of damage localization. Fig. 1 shows flowchart of proposed fusion imaging method, which comprises three core modules: adaptive dispersion compensation, dual-mode imaging fusion and CS-based sparse reconstruction.

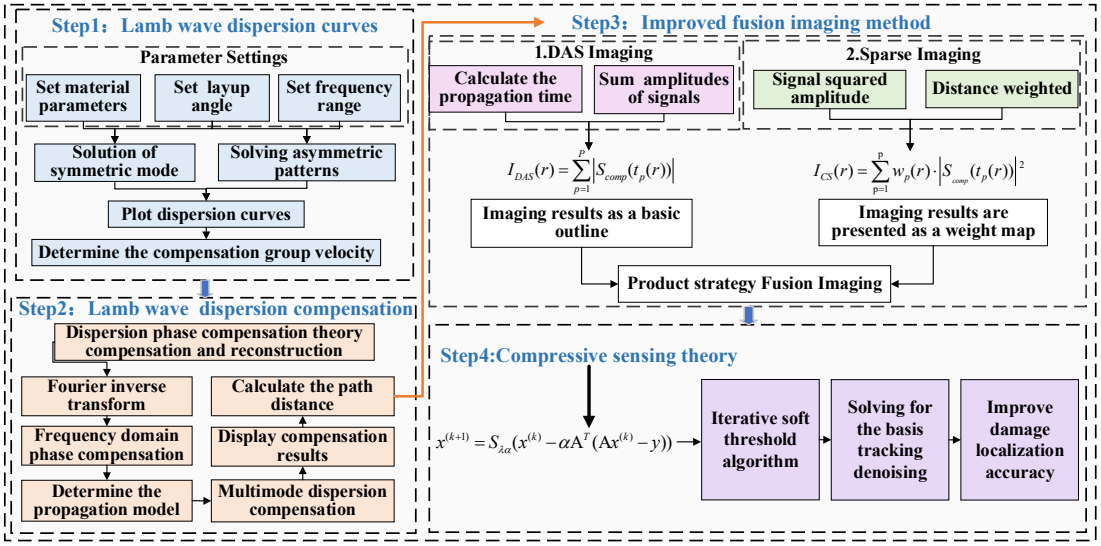

Fig. 1 Flowchart of the proposed fusion imaging method.

3. Finite element modeling and simulation for damage detection in CFRP Laminates

3.1 Solution for Lamb wave frequency dispersion curves

In this paper, the T300/5028 CFRP laminate is used as the specimen, with the following lay-up characteristics: a single-layer thickness of 0.125 mm, a total of 16 layers, and a layup pattern of $[0, 90, -45, 45]_{2s}$. The laminate has a symmetrical and balanced layup to minimize warpage induced by curing and to ensure the flat geometry required for simulation and experimental studies. These material parameters are presented in Table 3.

Table 3 Material properties of T300/5028 laminate.

Parameter	Value	Parameter	Value
Longitudinal Young's modulus E_1/(GPa)	132	Out-of-plane shear modulus G_{23}/(GPa)	5.65
Transverse Young's modulus E_2/(GPa)	10.5	Poisson's ratio v_{11}	0.24
Out-of-plane Young's modulus E_3/(GPa)	10.5	Poisson's ratio v_{12}	0.59
In-plane shear modulus G_{12}/(GPa)	5.65	Poisson's ratio v_{23}	0.24
Out-of-plane Shear modulus G_{13}/(GPa)	3.38	Density ρ/(kg/m^3)	1540

To validate the accuracy of the subsequent dispersion compensation algorithm, the precise propagation characteristics of Lamb waves within the specimen must first be determined. Based on material parameters provided in Table 3, Rayleigh-Lamb characteristic equation for multilayer anisotropic plates is solved numerically. This yields the dispersion curves for the S_0 and A_0 modes across the 0–500 kHz frequency range, as shown in Fig. 2. Fig. 3 presents the typical dispersion curve for the material along its principal axis (θ=0°). These results demonstrate that the group and phase velocities of modes S_0 and A_0 are clearly distinguishable and stable within the calculated frequency band. These curves are systematically compiled into a dispersion database. The

subsequent adaptive dispersion compensation algorithm can compute the propagation path direction angles from the sensor to potential damage points in real time. It can then rapidly interpolate the corresponding direction-dependent group velocity curves from the database to construct precise phase compensation factors. This approach theoretically accounts for the directional dependence of elastic wave propagation in anisotropic materials, such as carbon fiber composites, and provides the theoretical basis for subsequent precise dispersion compensation.

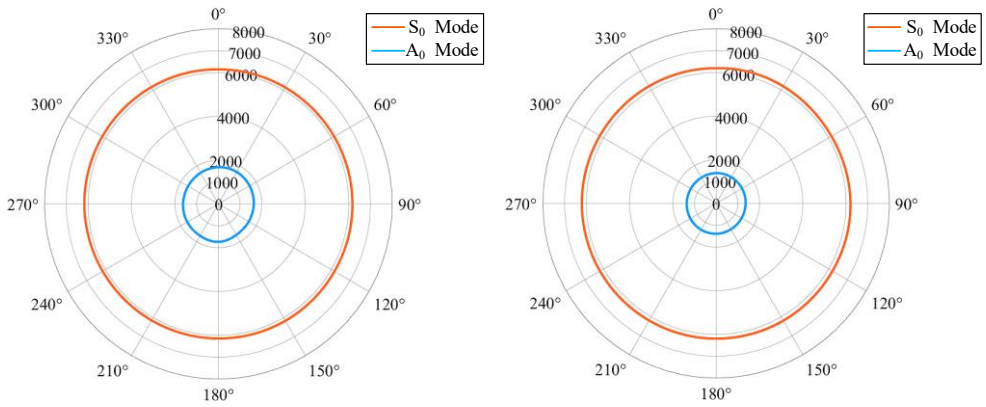

(a) (b)

Fig. 2 Polar plot of the Lamb wave dispersion curves for different propagation directions: (a) Phase velocity; (b) Group velocity.

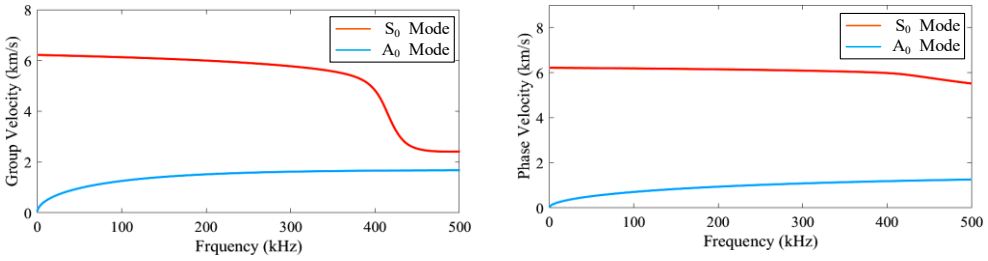

(a) (b)

Fig. 3 Dispersion curves of Lamb waves propagating at 0°: (a) Phase velocity; (b) Group velocity.

3.2 Finite element modeling and simulation

To validate the effectiveness of the proposed dispersion compensation method under complex physical conditions, a finite element model of a CFRP laminate with prefabricated delamination damage is established using Abaqus software. Numerical simulations are then performed to analyze the propagation of Lamb waves within the structure. The CFRP plate measure 300mm×300mm with a total thickness of 2mm. Fig. 4 shows a schematic diagram of the sensor layout and the location of the damage. The excitation and reception sensors are positioned on the surface of the CFRP laminate. As can be seen, sensor P1 serves as the excitation source, generating both symmetric and asymmetric Lamb wave modes by applying a concentrated normal force to the upper surface of the plate. Sensors P2-P8 serve as receivers, capturing the full wavefield response. As depicted in Fig. 4, two circular delamination zones, each with a diameter of 10mm, are pre-set between the 8th and 9th layers. Additionally, an elliptical delamination with major and minor axes of a=15mm and b=7.5mm, respectively, is located at coordinates (150, 150) mm. The centers of the circular delamination are located at coordinates (150, 150) mm and (100, 100) mm, respectively, while the center of the elliptical delamination is positioned at (100, 100) mm. Their precise locations are marked by red circles in the figures.

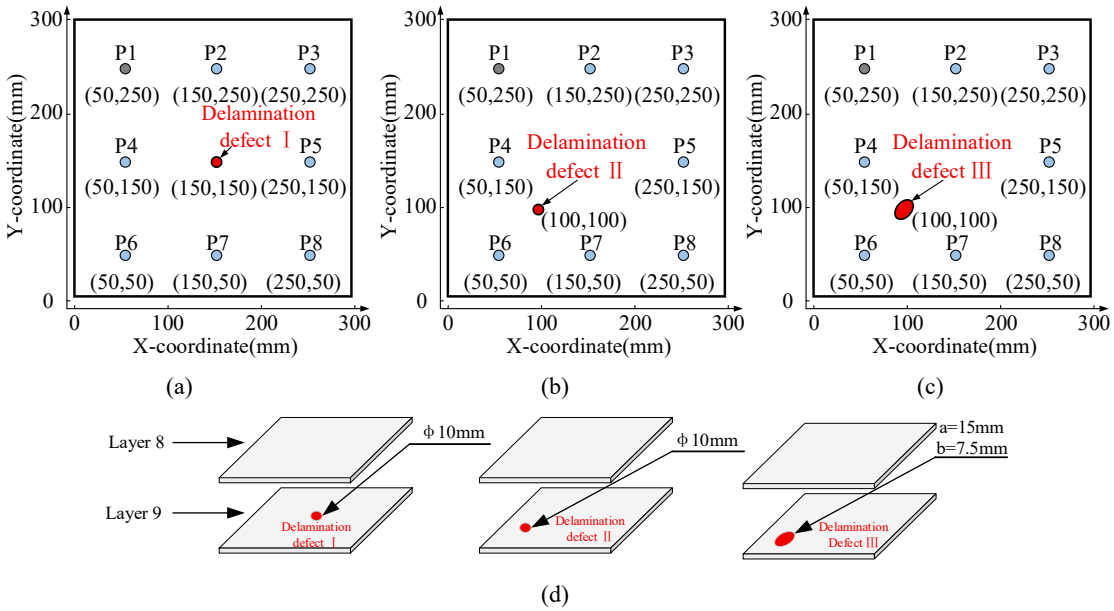

Fig. 4 Schematic of sensor layout and damage location: (a) Layout with circular damage at (150, 150); (b) Layout with circular damage at (100, 100); (c) Layout with elliptical damage at (150, 150); (d) Schematic of delamination damage location.

Due to attenuation trait of Lamb waves, the propagation process is highly sensitive to the internal structure and state of damage of the material. When Lamb waves undergo a delamination damage interface, significant reflection and refraction occur due to the abrupt change in material impedance. These phenomena result from alterations to the wave propagation path and local wave velocity caused by internal discontinuities. To visualize the dynamic interaction between Lamb waves and delamination damage across the full wavefield in CFRP plates, simulations are performed based on the sensor layout shown in Fig. 4, with out-of-plane displacement contours extracted from Abaqus. Fig. 5 presents wavefield snapshots at two characteristic time instants: 50μs and 140μs. At 50μs, the wavefront generated by the excitation source propagates outwards in a circular pattern, with most of the energy concentrated near the source. The wavefront appears clear and continuous. As the excitation is located on one side, the wavefield exhibits unidirectional propagation centered on the excitation source. By 140μs, the wavefront has reached to the predefined damage region. Distinct wavefield perturbations are visible at this stage: some of the energy continues to propagate forward (transmission), while another portion scatters due to the impedance discontinuity at the damage region, generating reflected waves that provide information about the location of the damage. Compared to bilateral excitation, the reflected waves under unilateral excitation primarily originate from the leading edge of the damage, and the wavefield interference pattern also emphasizes echo signals more strongly from the side of the excitation source.

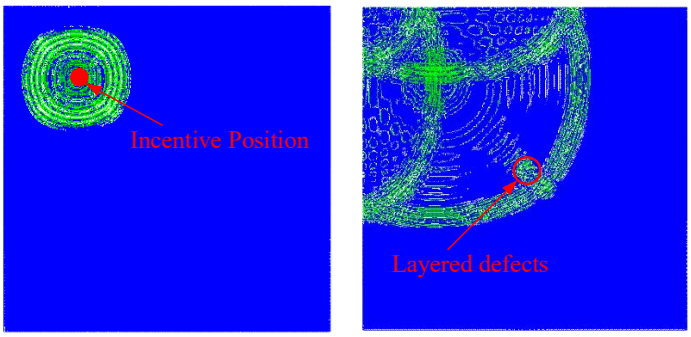

(a) (b)

Fig. 5 Displacement contour map of Lamb wave propagation at different time instants: (a) 50μs; (b) 140μs.

3.3 Lamb wave dispersion compensation

After preprocessing the acquired time-domain signals, the characteristic Lamb wave response shown in Fig. 6 is obtained. The first arriving wave packet, which corresponds to the direct wave, consists of a mixture of S_0 and A_0 modes. Based on the propagation distance and arrival time, the group velocities of the S_0 and A_0 modes are estimated to be approximately 6132m/s and 3487m/s, respectively. These values closely match the theoretical predictions shown in Fig. 2. Subsequent wave packets originate from damage scattering and exhibit more complex modal conversion phenomena. These packets can be decomposed further into sub-wave packets, which include scattered S_0 and A_0 modes, as well as mode-converted components generated at the damage site. Analysis of signals from different sensors shows that the S_0 scattering wave packet broadens moderately with increasing propagation distance, whereas the A_0 scattering packet broadens and attenuates in amplitude more pronouncedly due to its stronger dispersion. Therefore, applying dispersion compensation to the scattered signal is critical to restoring its initial focused state and providing high-quality data for subsequent high-precision imaging.

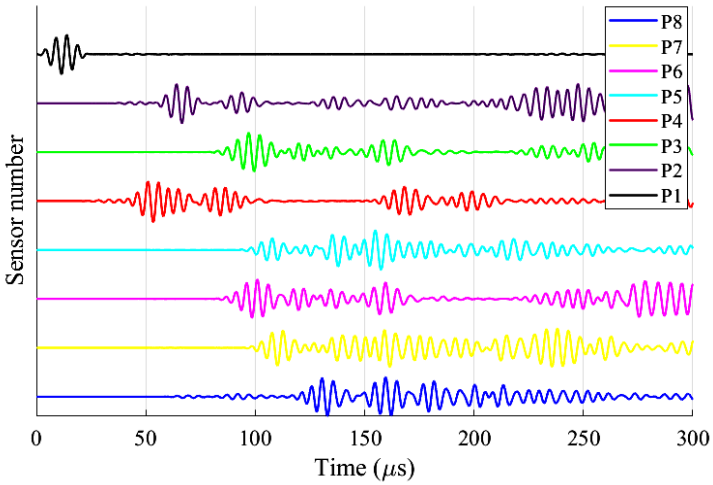

Fig. 6 Time-domain Lamb wave signals acquired at different sensor locations when the damage is located at (150, 150).

Based on the preceding analysis, when multimodal Lamb waves undergo full dispersion compensation, each modal signal will be optimally focused in the time domain. At this stage, the peak amplitude of the composite signal reaches its theoretical maximum value. This characteristic provides a basis for precise damage localization. In practical applications, the compensation distance corresponding to global peak amplitude of compensated signal is defined as effective

propagation distance between sensor and the damage, which is dynamically adjusted within a preset distance range.

To validate the effectiveness of this method, the simulation data for a case in which the damage is located at (150, 150) are analyzed first. Fig. 7 presents a comparison of the sensor signals before and after compensation. As can be seen, the compensated signals show a clear shift in the time domain of damage-scattered wave packets, with wave peaks becoming sharper and more pronounced. This result directly reflects the compensation algorithm's ability to correct dispersion effects through phase-delay adjustment. By precisely identifying the peak position, the effective distance propagation between each sensor and the damage can be calculated. As summarized in Table 4, maximum relative error between calculated and actual distances across all sensors is approximately 8%, which preliminarily demonstrates the accuracy of the compensation method.

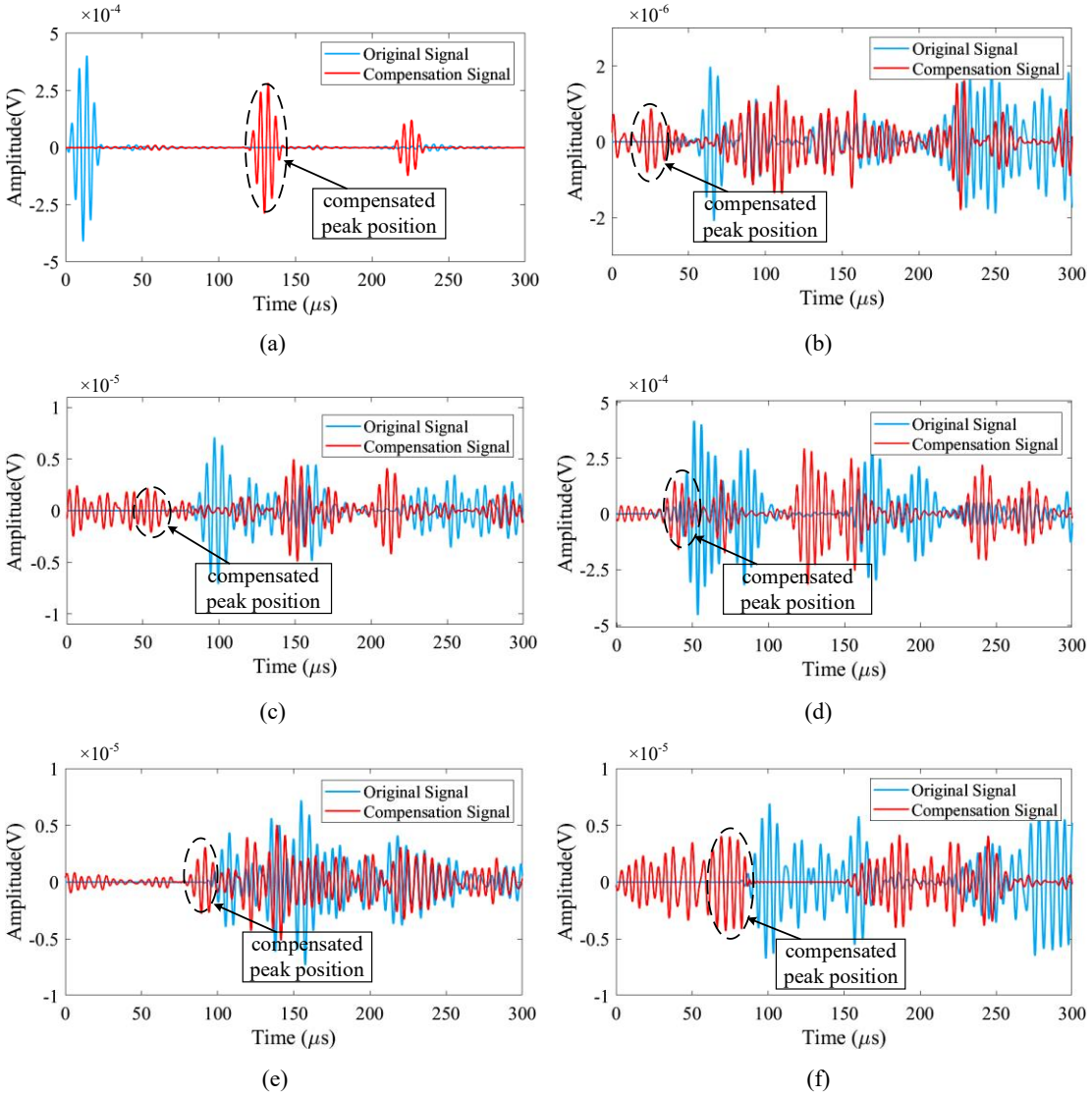

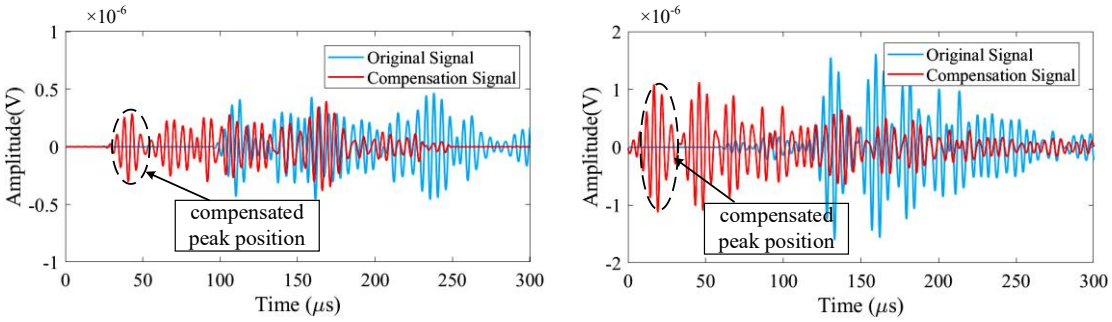

Fig. 7 Time-domain signal compensation results for each sensor with damage at (150, 150): (a) P1; (b) P2; (c) P3; (d) P4; (e) P5; (f) P6; (g) P7;(h) P8.

Table 4 Comparison of calculated and actual distances with damage at (150, 150) (mm).

Sensors	P1	P2	P3	P4	P5	P6	P7	P8
Actual distances	141.42	100	141.42	100	100	141.42	100	141.42
Calculated distances	145.67	104.45	136.89	96.23	104.12	146.78	95.67	147.68

To verify the effectiveness of this method under conditions of modal overlap and waveform distortion and for different damage locations, simulation data with damage located at (100, 100) is analyzed. To clearly illustrate the compensation effect, the first 3000 sampling points of the signal are extracted and the resulting time-domain waveform is presented in Fig. 8. As can be seen, even for a relatively long Lamb wave signal affected by significant modal interference, the proposed multimodal dispersion compensation method produces a clear focusing effect. The peak position of the compensated damage- scattered echo is clearly identifiable. The optimal compensated distance, calculated using Eq. (6), is summarized in Table 5. The results demonstrate minimal error from the actual distance, further highlighting the robustness of this method in scenarios involving complex damage configurations.

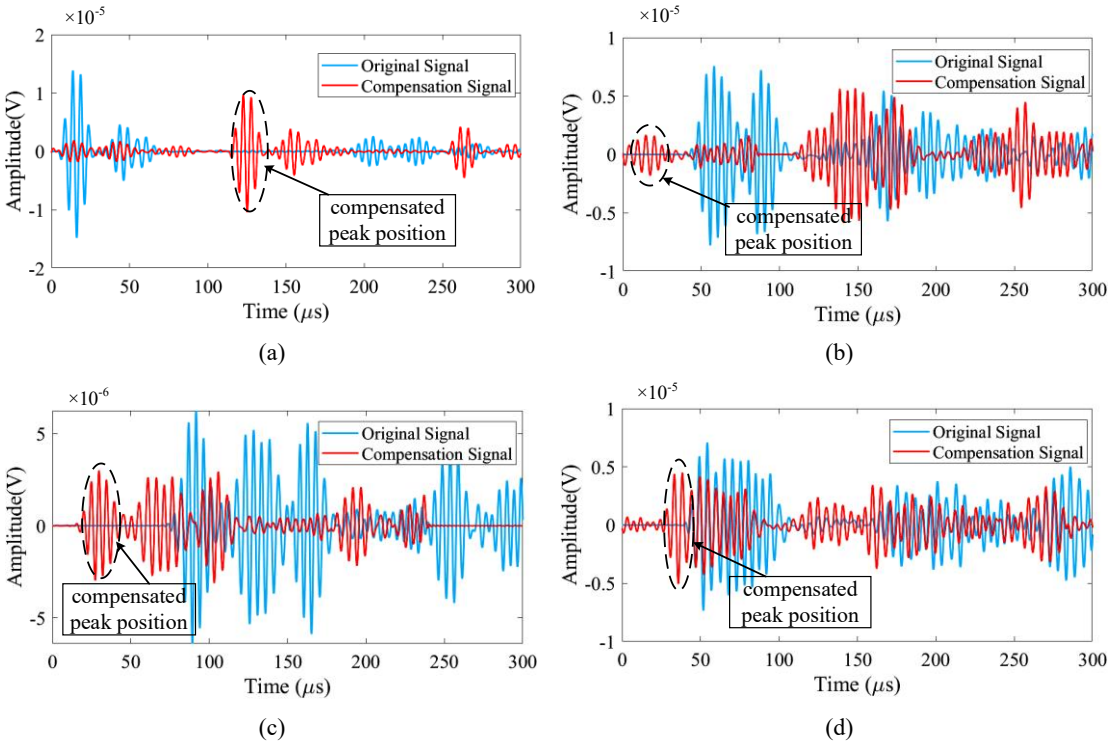

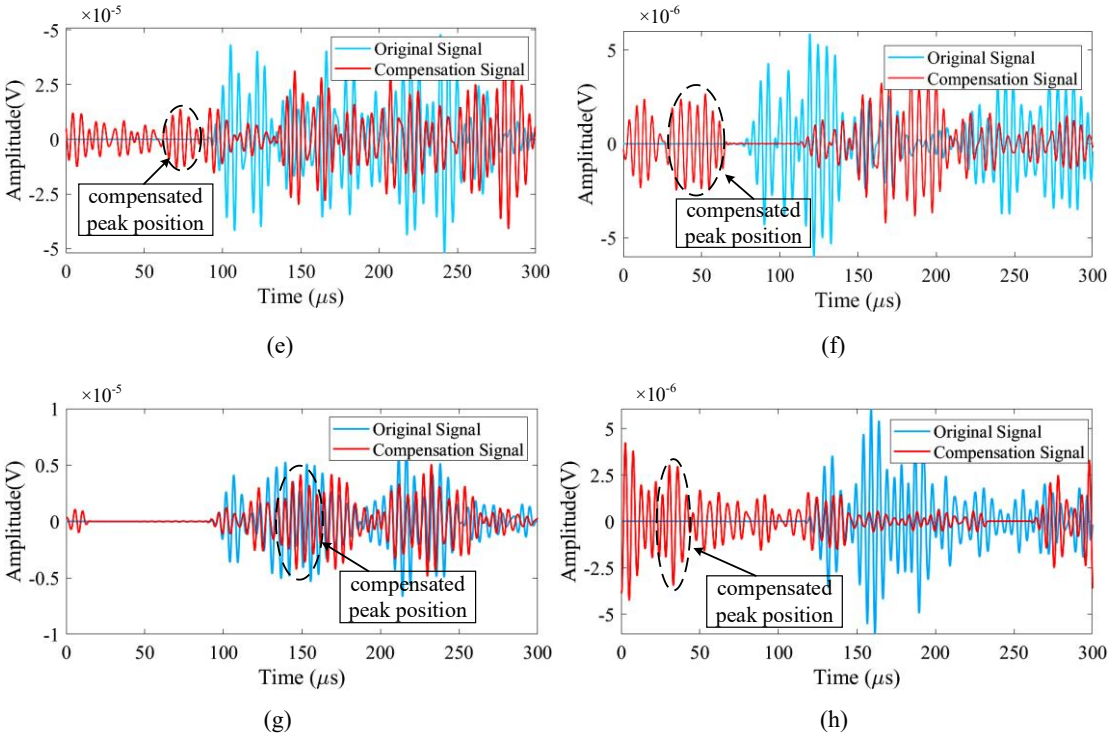

Fig. 8 Time-domain signal compensation results for each sensor with damage at (100, 100): (a) P1; (b) P2; (c) P3; (d) P4; (e) P5; (f) P6; (g) P7; (h) P8.

Table 5 Comparison of calculated and actual distances with damage at (100, 100) (mm).

Sensors	P1	P2	P3	P4	P5	P6	P7	P8
Actual distances	158.11	158.11	212.13	70.71	158.11	70.71	70.71	158.11
Calculated distances	163.32	152.58	218.76	74.45	163.87	74.23	75.12	152.34

3.4 Damage imaging and localization

Based on dispersion-compensated signals, the damaged regions are reconstructed using three methods: DAS imaging, CS imaging and the proposed method. This corresponding imaging results are presented in Figs. 9 and 10. It can be observed that although DAS imaging can roughly outline the damaged area, inherent algorithmic limitations hinder precise signal processing and accurate localization. Furthermore, due to Lamb wave dispersion and modal conversion effects, significant noise appears around the damage, further reducing imaging accuracy. CS imaging yields relatively concentrated energy at the damaged area; however, energy also accumulates in undamaged regions, creating spurious sources that severely compromise localization reliability. In contrast, the proposed method combines 30% DAS imaging features with 70% CS imaging features. The results demonstrate highly concentrated energy at the damaged area, forming sharp and distinct peaks that clearly indicates the position of the damage. Compared to the previous two methods, the proposed method effectively suppresses the noise artefacts inherent in DAS imaging and mitigates the false energy accumulation observed in CS imaging. This leads to a significant improvement in imaging accuracy and reliability. Furthermore, the proposed method achieves high-resolution imaging with a limited sensor array, demonstrating its potential for efficient and precise damage assessment in practical engineering applications.

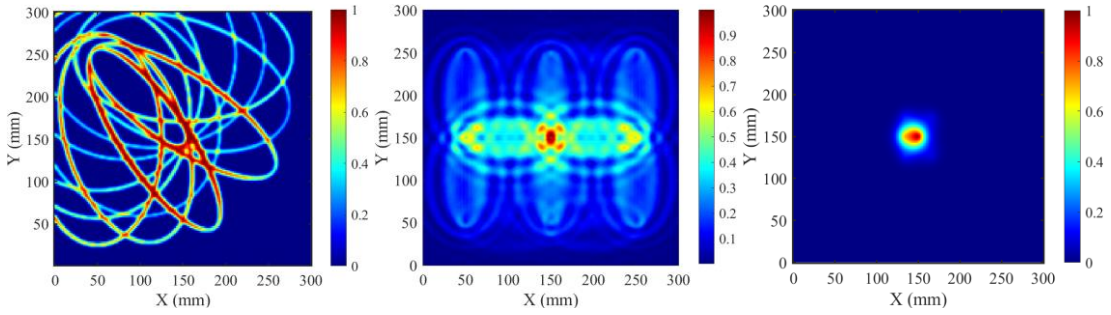

(a) (b) (c)

Fig. 9 Comparison of simulation imaging results with circular damage at (150, 150): (a) DAS; (b) CS; (c) Proposed method.

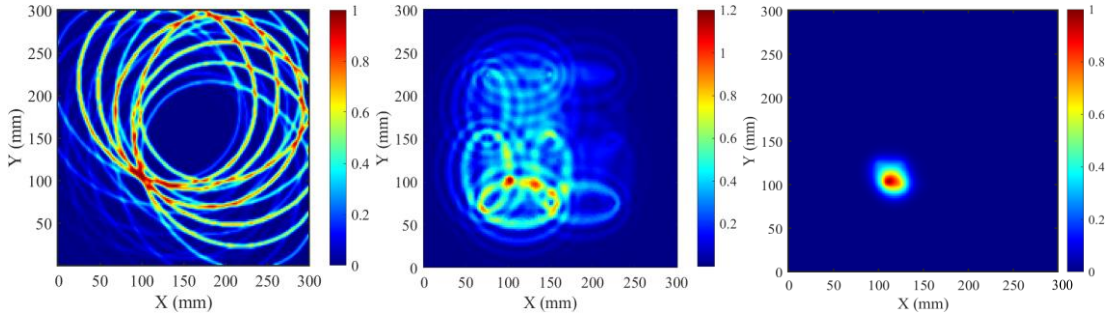

(a) (b) (c)

Fig. 10 Comparison of simulation imaging results with circular damage at (100, 100): (a) DAS; (b) CS; (c) Proposed method.

To better assess the robustness of the proposed method against variations in defect geometry, an elliptical delamination model is incorporated into the finite element simulations to represent the irregular damage geometries encountered in real structures. To enable consistent comparison, both defects are centered at coordinates (100, 100). Using the same sensor layout and signal-processing pipeline, the damage imaging results shown in Fig. 11 are obtained. These images confirm that the method accurately identifies the damaged area, with the reconstructed location closely matching the center of the actual damage.

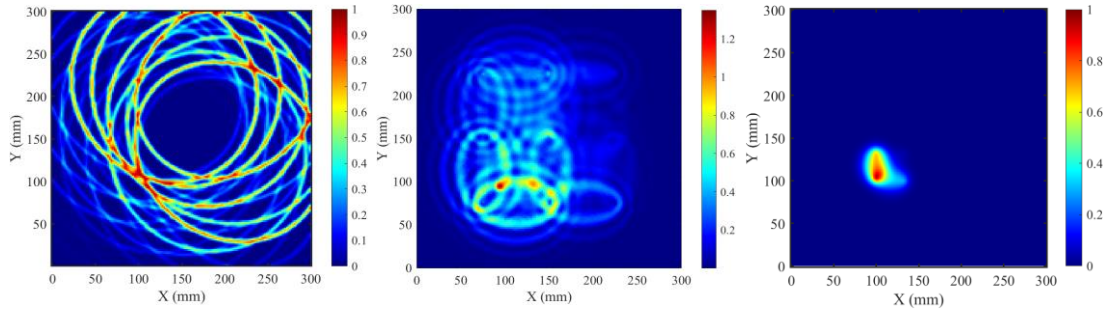

(a) (b) (c)

Fig. 11 Comparison of simulation imaging results with elliptical damage at (100, 100): (a) DAS; (b) CS; (c) Proposed method.

To further validate the proposed method, the RAPID imaging technique is incorporated as an additional control. Fig. 12 shows the corresponding RAPID imaging results. As can be seen, the damage-probability map shows the expected spatial probability distribution: a broad, relatively smooth zone of elevated probability around the preset damage location, following an approximately elliptical pattern whose major-axis orientation aligns with the sensor-array geometry. While the high-probability regions generally cover the actual damage site, the energy focusing is weak and

the images lack sharp, isolated damage peaks. Thus, although RAPID effectively identifies potential damage areas, it falls short in terms of precise localization. As illustrated in Fig. 12(c-d), thresholding extracts credible damage zones from the probability field by suppressing the low-probability background noise. However, the resulting contours remain diffuse and their geometric centers visibly deviate from the true damage coordinates.

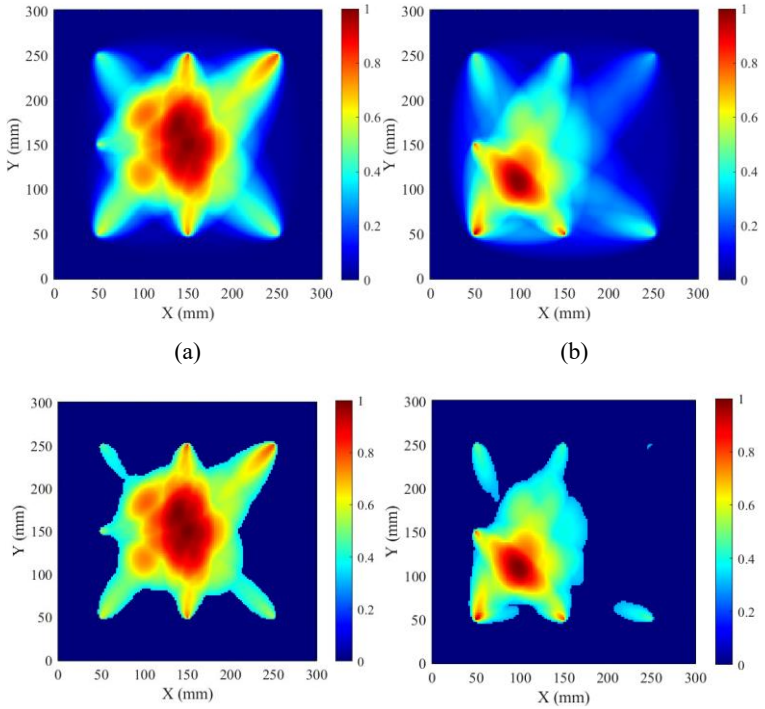

Fig. 12 Comparison of RAPID imaging results for simulated circular damage: (a, b) Original images for damage at (150, 150) and (100, 100); (c, d) Corresponding images after thresholding.

Based on the imaging results in Figs. 9-12, the corresponding localization results and errors are summarized in Tables 6 and 7. Localization error is defined as the Euclidean distance between the imaged and actual damage coordinates, reported as mean ± standard deviation across three sets of independent data in simulations. The results demonstrate that the proposed method achieves the highest localization accuracy in all three simulated cases, with a maximum error of 2.03±0.05mm. These results demonstrate the superiority of the proposed method and reveal the key limitations of traditional methods. Although DAS imaging is easy to implement and computationally efficient, its spatial blurring and sidelobe artefacts significantly reduce localization accuracy. CS imaging can achieve energy focusing, but it is highly sensitive to distance estimation errors and multiple scattering, which makes it prone to spurious peaks. RAPID relies on an elliptical probability model that assumes amplitude decays monotonically, which is rarely valid under strong dispersion and modal conversion. In summary, these findings suggest that anisotropic composite materials require a damage imaging approach that combines multimodal dispersion compensation with adaptive fusion.

Table 6 Damage localization results for different imaging methods (Simulation 1).

Imaging method	Actual location	Imaging positioning location	Error(mm)	Average error(mm)
DAS	(150, 150)	(147.6, 147.5)	3.47	3.27±0.17
		(148.0, 147.6)	3.12	
		(147.4, 148.1)	3.22	

CS	(150, 150)	(152.2, 147.6)	3.26	3.37±0.15
		(153.1 148.3)	3.54	
		(151.6, 147.1)	3.31	
RAPID	(150, 150)	(148.2, 152.8)	3.33	3.60±0.29
		(152.6, 152.9)	3.90	
		(152.2, 152.8)	3.56	
Proposed method	(150, 150)	(151.5, 148.6)	2.05	1.92±0.14
		(151.6, 148.9)	1.94	
		(151.3, 148.8)	1.77	

Table 7 Damage localization results for different imaging methods (Simulation 2, 3).

Imaging method	Actual location	Imaging positioning location	Error(mm)	Average error(mm)
DAS	Circular damage (100, 100)	(97.2, 97.6)	3.67	3.45±0.41
		(98.1, 97.7)	2.98	
		(97.3, 97.5)	3.67	
DAS	Elliptical damage (100, 100)	(97.4, 98.2)	3.00	3.39±0.35
		(97.2, 97.6)	3.67	
		(97.7, 102.6)	3.47	
CS	Circular damage (100, 100)	(97.2, 97.4)	3.82	3.50±0.71
		(98.1, 98.1)	2.69	
		(96.9, 97.5)	3.98	
CS	Elliptical damage (100, 100）	(102.4, 102.5)	3.47	3.77±0.27
		(102.8, 102.7)	3.89	
		(102.7, 102.9)	3.96	
RAPID	Circular damage (100, 100）	(102.8, 102.2)	3.56	3.84±0.44
		(102.4, 102.7)	3.61	
		(102.7, 103.4)	4.34	
Proposed method	Circular damage (100, 100）	(98.9, 98.7)	1.70	1.99±0.26
		(98.5, 98.6)	2.05	
		(98.2, 98.7)	2.22	
Proposed method	Elliptical damage (100, 100）	(98.5, 98.7)	1.99	2.03±0.05
		(98.8, 98.3)	2.08	
		(98.3, 98.9)	2.02	

4 Experimental validations

4.1 Experimental setup

In order to further validate effectiveness of this method, a hybrid detection experimental setup is constructed that integrated ultrasonic excitation and fiber Bragg grating (FBG) sensing, as illustrated in Fig. 13. This setup consists of two main modules: a signal excitation module and a sensing acquisition module. The signal excitation module comprises a Tektronix AFG2021-SC signal generator, an NF Circuit Design HAS-4052 power amplifier and a piezoelectric ceramic transducer (PZT) actuator that serves as the excitation source. The sensing acquisition module comprises an ASE broadband light source, an FPD610 photodetector, and a PCI Express data acquisition card for real-time acquisition of sensor response signals.

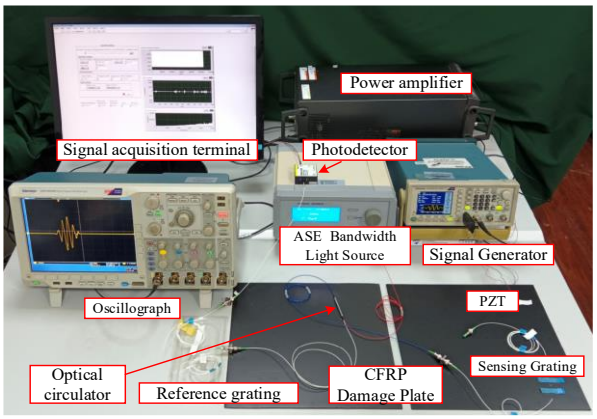

Fig. 13 Experimental setup.

A finite element simulation model has been established based on Section 3.2, two CFRP laminate specimens with pre-fabricated delamination damage are manufactured, as shown in Fig. 14. The experiment setup adopted a single-transmitter-multiple-receiver configuration, with the sensor layout matching the simulation geometry. Specifically, P1 serves as the PZT excitation source, using the same Lamb wave signal parameters as in the simulation. However, the bonded PZT excites multimodal Lamb waves, which differ from the ideal S_0-dominant excitation in simulations. Sensors P2 through P8 are deployed as FBG receivers. Throughout the experiments, the time-domain response signals from each sensing path are recorded in real time via a data acquisition card.

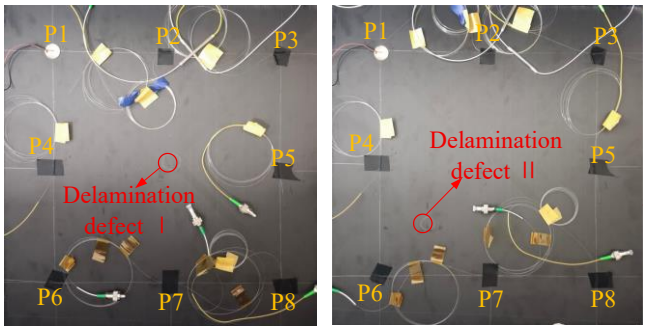

Fig. 14 Arrangement of the PZT actuator and FBG sensors.

4.2 Experimental results and analysis

Two CFRP laminate specimens with delamination damage located at (150, 150) and (100, 100), respectively, are tested experimentally. Lamb waves are excited by a PZT transducer at position P1, with the response signals captured by FBG sensors at positions P2 to P8. In composite structures, Lamb waves exhibit more pronounced dispersion characteristics, resulting in significant waveform broadening and distortion during propagation. Reflections and scattering induced by the damage introduce additional anomalies into the signals. To illustrate the effect of signal compensation at different propagation distances, the time-domain signals recorded by sensors P2 to P8 are plotted in Fig. 15.

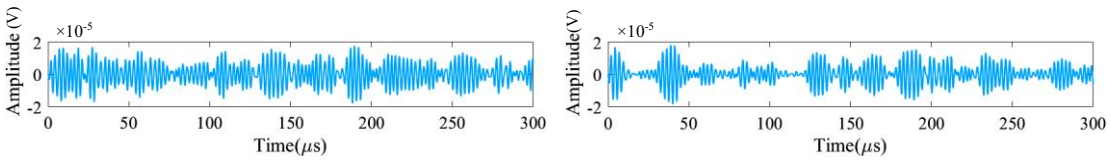

(a) (b)

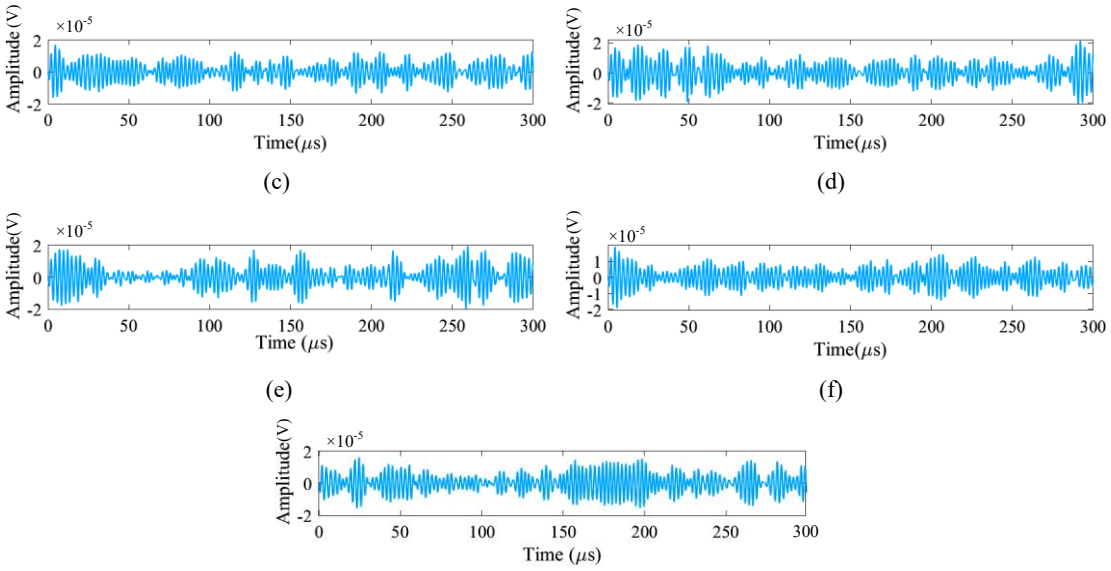

Fig. 15 Experimental time-domain waveforms recorded at sensor positions: (a) P2; (b) P3; (c) P4; (d) P5; (e) P6; (f) P7; (g) P8.

Dispersion compensation is applied to all Lamb signals along their respective excitation-reception paths using the same multimode phase compensation method as in the simulation. The optimal compensated distance between each sensor and the damaged area is calculated according to Eq. (6), based on peak amplitude of compensated packet. Fig. 16 shows the compensated signals recorded at sensor positions P2 to P8 for the specimen with damage at (150, 150). As can be seen, first packet in raw signal corresponds to artefact of excitation source, rather than first wave packet to arrive in propagation. Consequently, the compensated wave packets appear after the raw signal in the time domain. The validity of the compensation method is further confirmed by the calculated compensation distances, summarized in Tables 8 and 9.

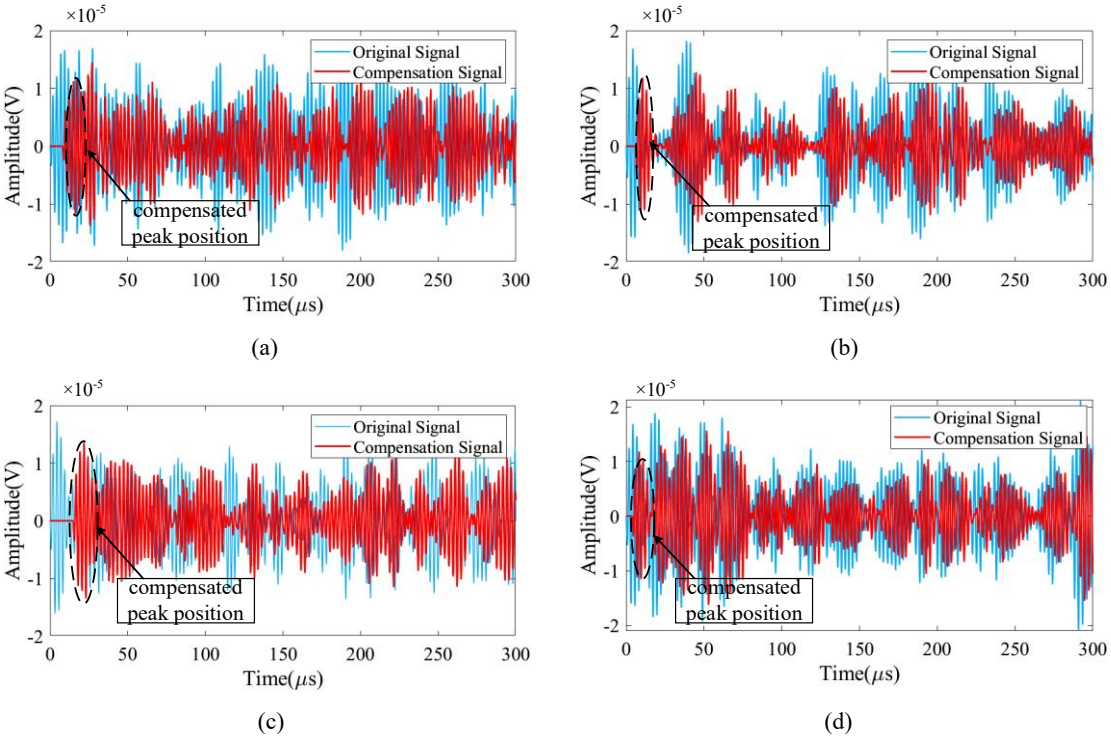

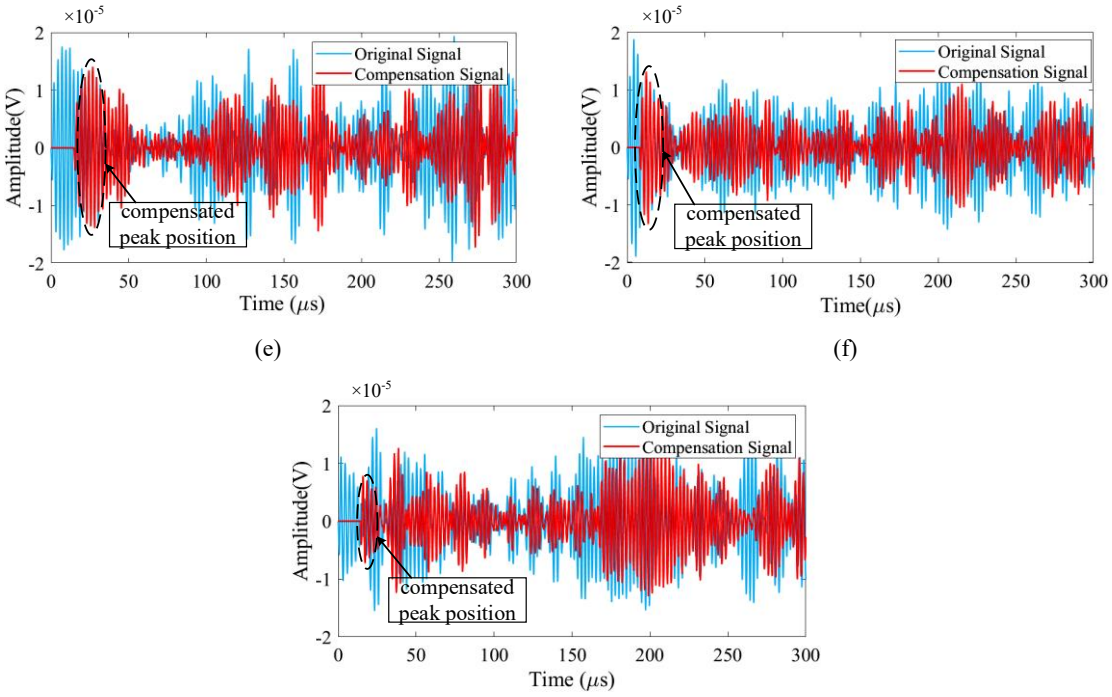

Fig. 16 Experimental time-domain signal compensation results for each sensor with damage at (150, 150): (a) P2; (b) P3; (c) P4; (d) P5; (e) P6; (f) P7; (g) P8.

Table 8 Comparison of calculated and actual distances with damage at (150, 150) (mm).

Sensors	P1	P2	P3	P4	P5	P6	P7	P8
Actual distance	141.42	100	141.42	100	100	141.42	100	141.42
Calculated distances	151.29	107.28	151.34	109.46	107.82	151.62	109.12	150.26

Table 9 Comparison of calculated and actual distances with damage at (100, 100) (mm).

Sensors	P1	P2	P3	P4	P5	P6	P7	P8
Actual distances	158.11	158.11	212.13	70.71	158.11	70.71	70.71	158.11
Calculated distances	163..24	164.73	220.67	78.42	163.29	77.83	79.42	165.28

The calculated dispersion-compensation distances are used to reconstruct the damage locations through three imaging methods: DAS imaging, CS imaging and proposed method. That results are presented in Figs. 17 and 18. Compared to the simulation results, the experimental DAS image shows greater interference around the damaged area due to increased signal noise, reducing imaging clarity and localization accuracy. In CS imaging, varying contributions from different sensor paths result in insufficient energy focusing along certain paths, which concentrates energy further in the undamaged areas. This effect is particularly evident when the damage is located at (100, 100), where the limited number of effective signal paths results in significantly higher localization error. In contrast, the proposed method yields a highly concentrated energy distribution at the actual damage location, even under experimental noise conditions. The imaging result shows a sharp and well-defined peak, demonstrating the method's strong noise robustness and its capability to accurate identify and localize damage.

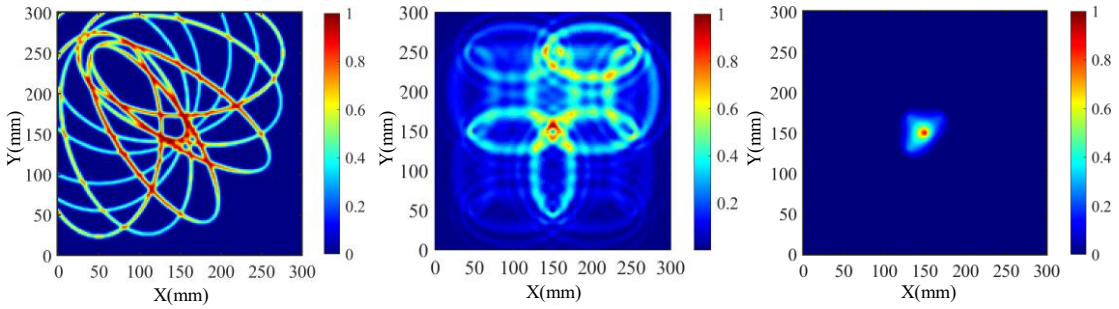

(a) (b) (c)

Fig. 17 Comparison of experimental imaging results with damage at (150, 150): (a) DAS; (b) CS; (c) Proposed method.

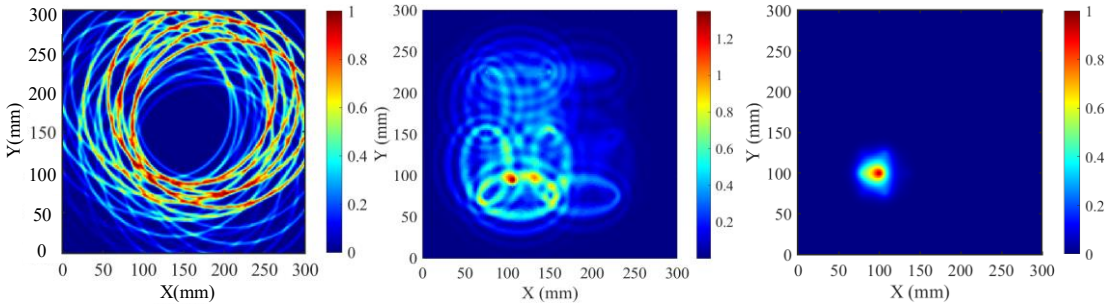

(a) (b) (c)

Fig. 18 Comparison of experimental imaging results with damage at (100, 100): (a) DAS; (b) CS; (c) Proposed method.

To further evaluate the performance of the proposed method, an additional experimental control in the form of the RAPID imaging technique was included. Fig. 19 shows the corresponding RAPID results. While RAPID can identify the damaged area to some extent, the probability field it generates shows a diffuse distribution: a broad, gently elevated zone around the damage with weak energy focusing and no sharp peaks. Thresholding improves the visibility of the damaged area, but the contours remain blurred and there is a visible offset between the geometric center and the true location, indicating limited localization accuracy. Compared with the simulation results, RAPID exhibits larger localization errors in experiments, primarily arising from experimental noise, material variability and amplified anisotropic propagation effects. The actual fiber orientation and layup of CFRP laminates introduce stronger anisotropy, leading to more complex Lamb wave directionality that deviates from the isotropic elliptical probability model assumed by RAPID. This introduces additional model error.

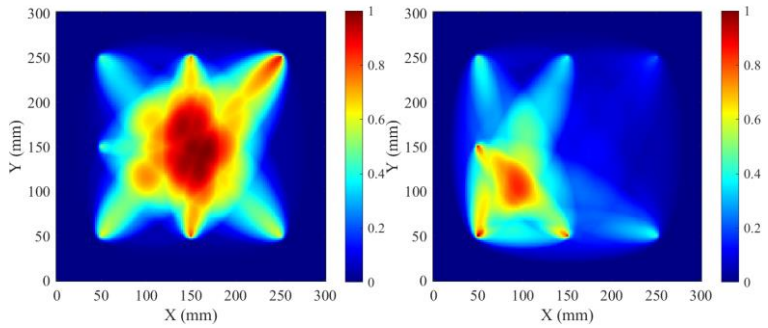

(a) (b)

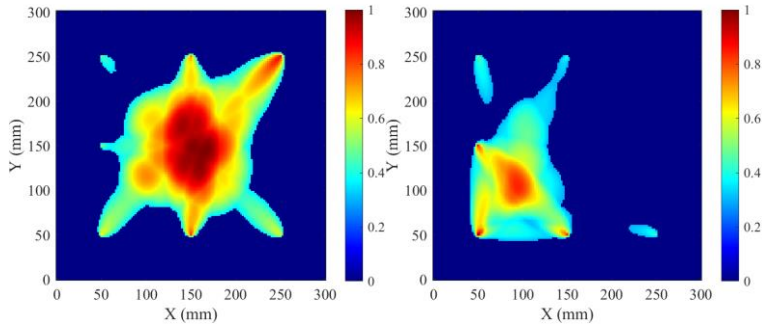

(c) (d)

Fig. 19 Comparison of experimental RAPID imaging results: (a, b) Original images for damage at (150, 150) and (100, 100); (c, d) Corresponding images after thresholding.

Based on the imaging results in Figs. 17-19, Tables 10 and 11 present the corresponding localization results and errors. As can be seen, the proposed method yields the smallest errors in both experimental cases, reaching a maximum localization error of only 2.31±0.56mm. The experimental results further emphasize the differences in performance between the various methods under real-world conditions, and demonstrate the effectiveness of the proposed method. By combining dispersion compensation with adaptive DAS and CS fusion, the method presented in this paper successfully suppresses artefacts while maintaining localization accuracy, even in non-ideal experimental conditions. These findings highlight the importance of combining physics-driven compensation mechanisms with sparse reconstruction to achieve reliable damage detection.

Table 10 Damage localization results for different imaging methods (Experiment 1).

Imaging method	Actual location	Imaging positioning location	Error(mm)	Average Error(mm)
DAS	(150,150)	(152.8, 152.3)	3.62	3.85±0.28
		(152.9, 153.0)	4.17	
		(152.7, 152.6)	3.75	
CS	(150, 150)	(147.7, 152.3)	3.25	3.43±0.20
		（147.6, 152.4）	3.39	
		(152.2, 152.9)	3.64	
RAPID	(150, 150)	(151.2, 153.3)	3.51	4.05±0.68
		(153.4, 153.4)	4.81	
		(152.8, 152.6)	3.82	
Proposed method	(150, 150)	(151.4, 152.0)	2.44	1.98±0.40
		(151.6, 150.8)	1.79	
		(148.9, 151.3)	1.70	

Table 11 Damage localization results for different imaging methods (Experiment 2).

Imaging method	Actual location	Imaging positioning location	Error(mm)	Average Error(mm)
DAS	(100,100)	(102.4, 98.4)	2.88	3.25±0.38
		(102.7, 97.8)	3.48	
		(102.6, 102.2)	3.40	
CS	(100, 100)	(102.4, 97.7)	3.32	3.50±0.42
		(102.4, 97.9)	3.19	
		(103.1, 97.5)	3.98	
RAPID	(100, 100)	(97.2, 103.2)	4.25	4.14±0.22
		(97.4, 103.4)	4.28	

		(97.2, 102.7)	3.89	
		(102.6, 101.4)	2.95	
Proposed method	(100, 100)	(101.2, 101.5)	1.92	2.31±0.56
		(101.5, 101.4)	2.05	

5 Conclusions and future work

5.1 Conclusion

This paper proposes a baseline-free damage imaging method that uses Lamb waves and integrates CS with multimodal dispersion compensation. The effectiveness and robustness of the method are verified through simulations and experiments. This research provides a feasible method to baseline-free, high-precision damage detection in composite structures, demonstrating significant potential for practical engineering applications. The main conclusions are summarized as follows:

(1) The dispersion curves of Lamb waves are computed based on the material parameters of the T300/5018 CFRP laminate, and adaptive compensation distances are obtained through compensation processing. The results demonstrate that the proposed method effectively compensates for multimodal Lamb wave dispersion, significantly reducing waveform broadening and signal distortion whilst enhancing signal resolution.

(2) Finite element simulations and experimental testing are conducted on CFRP laminates with delamination damage in different locations to validate the effectiveness of the proposed method in practical applications. These results demonstrate that the proposed method enables effective dispersion compensation for multimodal Lamb wave signals, and achieves high-precision damage detection in CFRP laminates.

(3) By integrating DAS imaging with sparse imaging within a CS theory based on basis pursuit denoising, the proposed method effectively improves signal quality and the capability to identify damage. This method is validated through simulations and experiments, achieving maximum localization errors of 2.03±0.05 in simulations and 2.31±0.56mm in experiments. It significantly reduces dispersion interference without the need for baseline signals, thereby significantly improving the accuracy and reliability of damage localization.

5.2 Limitations and future work

Although the proposed method is highly accurate and robust at locating delamination damage in CFRP laminates, further research is needed to overcome its limitations and increase its applicability in practical engineering settings. Future efforts will focus on the following areas.

(1) So far, the proposed method has only been simulated and experimentally validated for single circular delamination damage, while experimental verification for elliptical delamination is still pending. Future work will therefore focus on improving the method's ability to estimate the size and shape of the damage.

(2) Significant temperature variations can have a substantial impact on Lamb wave propagation, posing a challenge to the practical application of this technology. Subsequent work will involve conducting controlled temperature experiments and developing and integrating temperature compensation techniques to quantify the impact of thermal drift on localization accuracy.

(3) Although this study has primarily validated the detection performance under fixed sensor arrays, real-world engineering structures often involve more complex scenarios. Therefore, future work will focus on multi-damage identification and damage localization under sparse sensor

networks, while also advancing the development of corresponding anti-interference and high-resolution imaging strategies.

To advance the method towards practical deployment, subsequent work will involve integrating comprehensive physical models, developing intelligent algorithms and performing more systematic experimental validation.

Funding

This work was supported by the National Natural Science Foundation of China [Grant No. 52175518].

Disclosure statement

No potential conflict of interest was reported by the author(s).

Data availability

Data underlying the results presented in this paper are not publicly available at this time but may be obtained from the authors upon reasonable request.

References

[1] Gupta M, Khan M, Butola R, et al. Advances in applications of Non-Destructive Testing: A review[J]. Advances in Materials and Processing Technologies, 2022, 8(2): 2286-2307.

[2] Kot P, Muradov M, Gkantou M, et al. Recent advancements in Non-Destructive Testing techniques for Structural Health Monitoring[J]. Applied Sciences, 2021, 11(6): 2750.

[3] Wang B, Zhong S, Lee T, et al. Non-Destructive Testing and evaluation of composite materials/structures: A state-of-the-art review[J]. Advances in mechanical engineering, 2020, 12(4): 1687814020913761.

[4] Jodhani J, Handa A, Gautam A, et al. Ultrasonic non-destructive evaluation of composites: A review[J]. Materials Today: Proceedings, 2023, 78: 627-632.

[5] Jiao P, Egbe K, Xie Y, et al. Piezoelectric sensing techniques in Structural Health Monitoring: A state-of-the-art review[J]. Sensors, 2020, 20(13): 3730.

[6] Rocha H, Semprimoschnig C, Nunes J. Sensors for process and Structural Health Monitoring of aerospace composites: A review[J]. Engineering Structures, 2021, 237: 112231.

[7] Arnold W, Goebbels K, Kumar A. Ultrasonic non-destructive materials characterization[M]. Non-destructive Materials Characterization and Evaluation. Berlin, Heidelberg: Springer Berlin Heidelberg, 2023.

[8] Li J, Han Y. Dispersion compensation method for lamb waves based on measured wavenumber[J]. Shock and Vibration, 2020(1): 6704642.

[9] Wilcox P, Lowe M, Cawley P. Lamb and SH wave transducer arrays for the inspection of large areas of thick plates[C]. Montreal: American Institute of Physics, 2000, 509(1): 1049-1056.

[10] Cai J, Yuan S, Wang T. Signal construction-based dispersion compensation of lamb waves considering signal waveform and amplitude spectrum preservation[J]. Materials, 2016, 10(1): 4.

[11] Jochen M, Luca M, Christian K, et al. High resolution defect imaging in guided waves inspections by dispersion compensation and nonlinear data fusion[J]. Acta Acustica united with Acustica,2017,103(6): 941-949.

[12] Zhang H, Hua J, Tong T, et al. Dispersion compensation of Lamb waves based on a convolutional auto-encoder[J]. Mechanical Systems and Signal Processing, 2023, 198: 110432.

[13] Li S, Yang Z, Zeng J, et al. A novel dispersion compensation of Lamb waves by nonlinear group delay estimation for defect imaging[J]. IEEE Transactions on Instrumentation and Measurement, 2025, 74: 9503710.

[14] Ling F, Chen H, Lang Y, et al. Lamb wave tomography for defect localization using wideband dispersion reversal method[J]. Measurement, 2023, 216: 112965.

[15] De Marchi L, Ruzzene M, Xu B, et al. Warped basis pursuit for damage detection using lamb waves[J]. IEEE Transactions on Ultrasonics, Ferroelectrics, and Frequency Control, 2010, 57(12): 2734-2741.

[16] Zeng L, Lin J. Chirp-based dispersion pre-compensation for high resolution Lamb wave inspection[J]. NDT & E International, 2014, 61: 35-44.

[17] Xu C, Yang Z, Chen X, et al. A guided wave dispersion compensation method based on compressed sensing[J]. Mechanical Systems and Signal Processing, 2018, 103: 89-104.

[18] Su C, Jiang M, Liang J, et al. Damage identification in composites based on Hilbert energy spectrum and Lamb wave tomography algorithm[J]. IEEE Sensors Journal, 2019, 19(23): 11562-11572.

[19] Luo Kai, Chen Liang, Chen Yuan, et al. An ultrasonic Lamb wave-based non-linear exponential RAPID method for delamination detection in composites[J]. Composite Structures, 2025, 352: 118701.

[20] Migot A, Bhuiyan Y, Giurgiutiu V. Numerical and experimental investigation of damage severity estimation using Lamb wave–based imaging methods[J]. Journal of Intelligent Material Systems and Structures, 2019, 30(4): 618-635.

[21] Sicard R, Goyette J, Zellouf D. A SAFT algorithm for lamb wave imaging of isotropic plate-like structures[J]. Ultrasonics, 2002, 39(7): 487-494.

[22] Wang B, Shi W, Zhao B, et al. Detecting delamination defects in CFRP plates using nonlinear defect index of air-coupled Lamb waves and adaptively weighted imaging algorithm[J]. Mechanical Systems and Signal Processing, 2024, 208: 111023.

[23] Xu C, Deng M. Lamb wave imaging based on multi-frequency sparse decomposition[J]. Mechanical Systems and Signal Processing, 2022, 174: 109076.

[24] Muller A, Robertson-Welsh B, Gaydecki P, et al. Structural Health Monitoring using lamb wave reflections and total focusing method for image reconstruction[J]. Applied Composite Materials, 2017, 24(2): 553-573.

[25] Cui X, Song B, Li D, et al. A Baseline-Free Lamb Wave Damage Localization Method Based on Compressed Sensing[J]. Structural Control and Health Monitoring, 2023(1): 5748724.

[26] Perelli Alessandro, Di Ianni, Marzani Alessandro, et al. Model-based compressive sensing for damage localization in lamb wave inspection[J]. IEEE Transactions on Ultrasonics, Ferroelectrics, and Frequency Control, 2013, 60(10): 2089-2097.

[27] Hora P, Červená O. Determination of Lamb wave dispersion curves by means of Fourier transform[J]. Applied and Computational Mechanics, 2012, 6(1): 5-16.

[28] Kijanka P, Radecki R, Packo P, et al. GPU-based local interaction simulation approach for simplified temperature effect modelling in Lamb wave propagation used for damage detection[J]. Smart Materials and STRUCTURES, 2013, 22(3): 035014.

[29] Yu Y, Liu X, Wang Y, et al. Lamb wave-based damage imaging of CFRP composite structures using autoencoder and Delay-and-Sum[J]. Composite Structures, 2023, 303: 116263.

[30] Hua J, Gao F, Zeng L, et al. Modified sparse reconstruction imaging of lamb waves for damage quantitative evaluation[J]. NDT & E International, 2019, 107: 102143.

[31] Beck A, Teboulle M. A fast iterative shrinkage-thresholding algorithm for linear inverse problems[J]. SIAM Journal on Imaging Sciences, 2009, 2(1): 183-202.